

Nodal Topological Superconductivity in Monolayer NbSe₂

Wen-Yu He, Benjamin T. Zhou, James J. He, Ting Zhang and K. T. Law*

Department of Physics, Hong Kong University of Science and Technology, Clear Water Bay, Hong Kong, China

Recently, it was shown that the in-plane upper critical field H_{c2} of superconducting monolayer NbSe₂ can be six times higher than the Pauli limit field. This is due to the Ising spin-orbit coupling (SOC) which pins electron spins to the out-of-plane directions and protects the electron spins from being aligned to the in-plane directions. In this work, we show that in a wide range of experimentally accessible regimes where the in-plane magnetic field is higher than the Pauli limit field but lower than H_{c2} , a monolayer NbSe₂ becomes a nodal topological superconductor. The bulk nodal points appear on the $\Gamma - M$ lines of the Brillouin zone where the Ising SOC vanishes. The nodal points are connected by Majorana flat bands, similar to the Weyl points being connected by surface Fermi arcs in Weyl semimetals. The Majorana flat bands are associated with a large number of zero energy Majorana fermion edge modes which induce spin-polarized Cooper pairs on the edges. The detection of this nodal topological phase in transport experiments is discussed.

Introduction

A monolayer transition metal dichalcogenide (TMD), formed by a layer of transition metal atoms sandwiched between two layers of chalcogen atoms in the trigonal prismatic structure [1], possesses remarkable electronic and optical properties. Because of its two-dimensional nature, high electron mobility and massive Dirac energy spectrum, TMD materials are considered candidates for next generation transistors [2–6]. Moreover, due to in-plane mirror symmetry breaking and strong atomic spin-orbit coupling (SOC), the material possesses a special type of SOC we referred to as Ising SOC [7–9] to distinguish it from Rashba SOC [10] which pins electron spins to in-plane directions. Ising SOC acts as an effective Zeeman field which pins spins to opposite out-of-plane directions for electrons with opposite momentum. The energy splitting due to Ising SOC can be as high as 450meV in tungsten based monolayer TMDs near the K points [2, 11, 12]. Novel optical and transport phenomena related to this spin-momentum locking are under intense study [14–16].

Moreover, several semiconducting TMD thin films, such as MoS₂, MoSe₂ and WS₂ are found to be superconducting [7, 17–20] under electro-gating. Importantly, the in-plane upper critical fields H_{c2} of these systems such as MoS₂ can be several times higher than the Pauli limit fields, depending on the gating strength. It was explained that Ising SOC pins electron spins to the out-of-plane directions, preventing the electron spins from being aligned with in-plane magnetic fields and hence protects the superconductivity [7, 20]. It was shown more recently that the Ising superconductors can be used to engineer Majorana fermions due to the strong Ising SOC [9, 21, 22].

Parallel to the development in gated semiconducting TMDs, monolayers of NbSe₂ have been successfully fabricated and exhibit superconductivity with the critical temperature at around 3K [8, 23–25]. Unlike MoS₂, NbSe₂ are intrinsic superconductors and the chemical po-

tential lies in the top valence band as depicted in Fig.1b. It was found experimentally that the H_{c2} can be as high as 35T, which is about 6 times the Pauli limit field [8]. By solving the self-consistent gap equations for NbSe₂, taking into account the realistic band structures, we show in Fig.1d that H_{c2} of the system is much higher than the Pauli limit. An important remaining question is: what happens to the superconducting state when the external field is stronger than the Pauli limit but lower than H_{c2} ? As shown in Fig.1d, this regime occupies a large part of the phase diagram and it is easily accessible experimentally.

In this work, we show that when the applied in-plane magnetic field is slightly higher than the Pauli limit, the superconducting gap in the energy spectrum is closed by the magnetic field and the system goes through a topological phase transition from a fully gapped s-wave pairing phase to a nodal topological superconducting phase. The nodal points in the Brillouin zone are depicted in Fig.2a. The nodal points are connected by Majorana flat bands in the energy spectrum as shown in Fig.2b, similar to the case of Weyl semimetals in which the Weyl points are connected by the surface Fermi arcs [26–28]. The study of nodal topological phase has been a central topic in physics recently. We believe that superconducting TMD materials such as monolayer NbSe₂ are promising candidates for the realization of nodal topological superconductors.

In the following section, we first present the band structure of a monolayer NbSe₂ calculated by density functional theory (DFT) method and construct a tight-binding model which can well describe the DFT calculations. Secondly, using the tight-binding model, we explain the origin of the enhanced in-plane H_{c2} in NbSe₂. Thirdly, we discuss how the nodal topological phase can be induced by an in-plane magnetic field resulting in nodal points which are connected by Majorana flat bands. Finally, we study how to detect this topological

nodal phase by tunnelling experiments.

Results

Band structure in normal state— A monolayer NbSe₂ is formed by a layer of Nb atoms with triangular lattice sandwiched by two layers of Se atoms with triangular lattices. The material has a hexagonal lattice structure when viewed from the out-of-plane direction but with broken A-B sublattice symmetry as shown in Fig.1a. Therefore, an in-plane mirror symmetry along y direction is broken and this gives rise to the Ising SOC which pins electron spins to the out-of-plane directions and split the energy bands [29]. The band structure of a monolayer NbSe₂ is obtained through first-principle calculations taking into account SOC using *ABINIT* package [30]. The results are presented in Fig.1b. As expected, the shape of the band structure is almost identical to the band structures of monolayer MoS₂, MoSe₂, WSe₂ and WTe₂ found in previous works [2]. However, unlike Mo and W based materials which are insulating intrinsically, a Nb atom has one less *d*-electron in the outer most shell than Mo and W atoms and the chemical potential of NbSe₂ lies in the valence band. The band splitting at the K points due to Ising SOC is about 150meV. Importantly, the band splitting is significant at the Fermi energy even the Fermi surface is far away from the K points. As we show in the next section, this Ising SOC at the Fermi energy plays a crucial role in protecting the superconductivity from the paramagnetic effects of in-plane magnetic fields.

In order to study the superconducting properties of the material, we construct a six-band tight-binding model which consists of the d_{z^2} , d_{xy} and $d_{x^2-y^2}$ orbitals [1, 2] of the Nb atoms. Including the third-nearest-neighbor hoppings, this band structure of the DFT calculations can be well explained. The details of the tight-binding model $H_N(\mathbf{k})$ and the fitting parameters can be found in the Method Section and the Supplementary Material [32]. The Fermi surfaces from the tight-binding model are shown in Fig.1c. At the Fermi level, there are Fermi pockets around Γ , K and -K points. In general, the bands are split by Ising SOC except for the states lying along the $\Gamma - M$ lines.

Ising superconductivity in monolayer NbSe₂

It is well-known that bulk NbSe₂ is superconducting with T_c of 7K [33]. However, monolayer NbSe₂ was shown to be superconducting only very recently with T_c on-set at about 5K and zero resistance appears at about 3K [8, 23–25]. In bulk NbSe₂, magnetic field can create vortices which eventually destroy superconductivity with H_{c2} of about 14.5T [34]. In the monolayer case, the orbital effects of in-plane magnetic fields are completely suppressed and the magnetic field can suppress superconductivity only through Zeeman coupling with electron spins.

Similar to the gated superconducting MoS₂, NbSe₂ was shown to have strongly enhanced H_{c2} at 35T even though

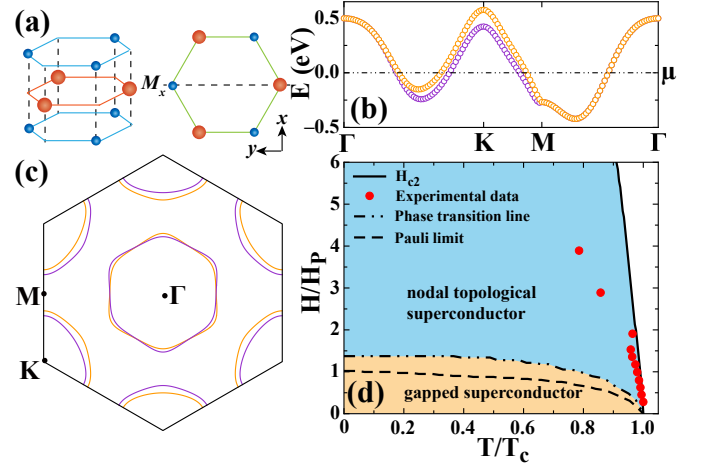


FIG. 1: (a) Lattice structure of monolayer NbSe₂ (left) and its top view (right). M_x denotes the in-plane mirror symmetry. (b) The band structure for the normal state of monolayer NbSe₂ from DFT calculations. (c) The energy contour at the Fermi level from tight-binding model. (d) The H-T phase diagram of the monolayer NbSe₂. The red dots represent the experimental data from Ref. [8]. The calculated H_{c2} is denoted by the solid line and it is much higher than the Pauli limit which is denoted by the dashed line. When the applied in-plane magnetic field is higher than the Pauli limit but lower than H_{c2} , the system can go through a phase transition from a fully gapped superconducting phase to a nodal topological phase.

the T_c is much lower than the bulk T_c . While the experimental data in MoS₂ can be well explained by solving the self-consistence gap equations by taking into account the Ising SOC and Rashba SOC induced by gating, a microscopic theory for explaining the H_{c2} data of monolayer NbSe₂ is still lacking due to the more complicated band structures in the valence bands. In this work, with the tight-binding model introduced in the Method Section, we can take into account all the three Fermi pockets shown in Fig.1c to explain the experimental data. An intra-orbital attractive interaction U [32] between the electrons is introduced. U is determined by the self-consistent gap equation $\Delta = -U/V \sum_{\mathbf{k},o} \langle c_{\mathbf{k},\downarrow,o} c_{-\mathbf{k},\uparrow,o} \rangle$ at zero magnetic field. Here, $\Delta = 1.76k_B T_c$ is the pairing gap at zero temperature, V is the area of the sample and $c_{\mathbf{k},\uparrow/\downarrow,o}$ is the electron annihilation operator for orbital o .

After finding U at zero magnetic field, we can determine Δ as a function of magnetic field by minimizing the free energy density

$$\Omega = |\Delta|^2/U - \frac{1}{V} \sum_{\mathbf{k},n} \frac{1}{2\beta} \ln(1 + e^{-\beta E_{\mathbf{k},n}}) \quad (1)$$

with $E_{\mathbf{k},n}$ the eigenvalue adopted from the Bogoliubov-de Gennes Hamiltonian H_{BDG} as shown in detail in the Supplementary Material [32]. The phase diagram for this Ising superconductor is determined and shown in Fig.1(d), with $H_p \approx 1.84T_c$ the Pauli limit [35]. As shown

in Fig.1(d), the calculated H_{c2} (solid line) is strongly enhanced. The theoretical values of H_{c2} , using the parameters from the tight-binding model without any tuning parameters, are higher than the experimental values (the red dots). Such discrepancy can be due to the fact that the NbSe₂ sample has ripples [36], and the ripples introduce Rashba type SOC [37] which competes with Ising SOC. This Rashba type SOC can lower the in-plane H_{c2} as in the case of gated superconducting MoS₂ [7]. We ignore the effects of ripples in this work. To highlight the importance of Ising SOC, the H_{c2} in the absence of Ising SOC is denoted by the dashed line in Fig.1(d). It is evident that the Ising SOC enhances H_{c2} so that it becomes much higher than the Pauli limit.

Nodal topological phase— From Fig.1d, one can see that superconductivity survives in the regime where the applied magnetic field is higher than the Pauli limit field. The question is: what are the properties of the superconducting phase under strong magnetic fields? To answer this question, the spectral function $A(E, \mathbf{R}) = -\frac{1}{\pi} \text{Tr} [\text{Im} G(E, \mathbf{R})]$ of the a semi-infinite NbSe₂ stripe is shown in Fig.2b. Here, E is energy and \mathbf{R} is a point on the armchair edge and G is the Green's function of the BdG Hamiltonian defined in Supplementary Material [32]. The armchair edges are parallel to the y -direction and subject to periodic boundary conditions. The in-plane magnetic field applied is chosen to be $H = 3H_p$. It can be seen that there are four sections of Majorana flat bands in Fig.2a. The Majorana flat bands connect the four pairs of bulk nodal points. These four pairs of nodal points are projections of the six pairs of bulk nodal points in the bulk energy spectrum as shown in Fig.2a.

To understand this nodal topological phase, we use an effective Hamiltonian approach and understand the system from a symmetry point of view. Before writing down the effective Hamiltonian near the Fermi energy, we note that the Ising SOC near the K points is very strong as shown in Fig.1b. Therefore, the superconducting states near K points are hardly affected by the in-plane magnetic field at $H = 3H_p \ll H_{c2}$. Therefore, to understand the gap closing effect of the in-plane magnetic field, we only need to focus on the states in the Γ pocket where Ising SOC is weaker.

Around the Γ pocket, the d_{z^2} orbital dominates [1, 2]. In the basis of $[c_{k,\uparrow}, c_{k,\downarrow}]$ and in the absence of external magnetic fields, the Hamiltonian has to satisfy the point group symmetries $M_z = -i\sigma_z$, $M_x = -i\sigma_x$, $C_3 = e^{-i\frac{\pi}{3}\sigma_z}$ and time-reversal symmetry $T = i\sigma_y K$. These symmetries restrict the effective Hamiltonian, up to third order in k , to have the form:

$$\mathcal{H}_0 = \left[\frac{k_x^2 + k_y^2}{2m} - \mu \right] \sigma_0 + \lambda_{\text{SOC}} (k_+^3 + k_-^3) \sigma_z. \quad (2)$$

Here, μ is the chemical potential and $k_{\pm} = k_x \pm ik_y$. It is important to note that λ_{SOC} term vanishes along the

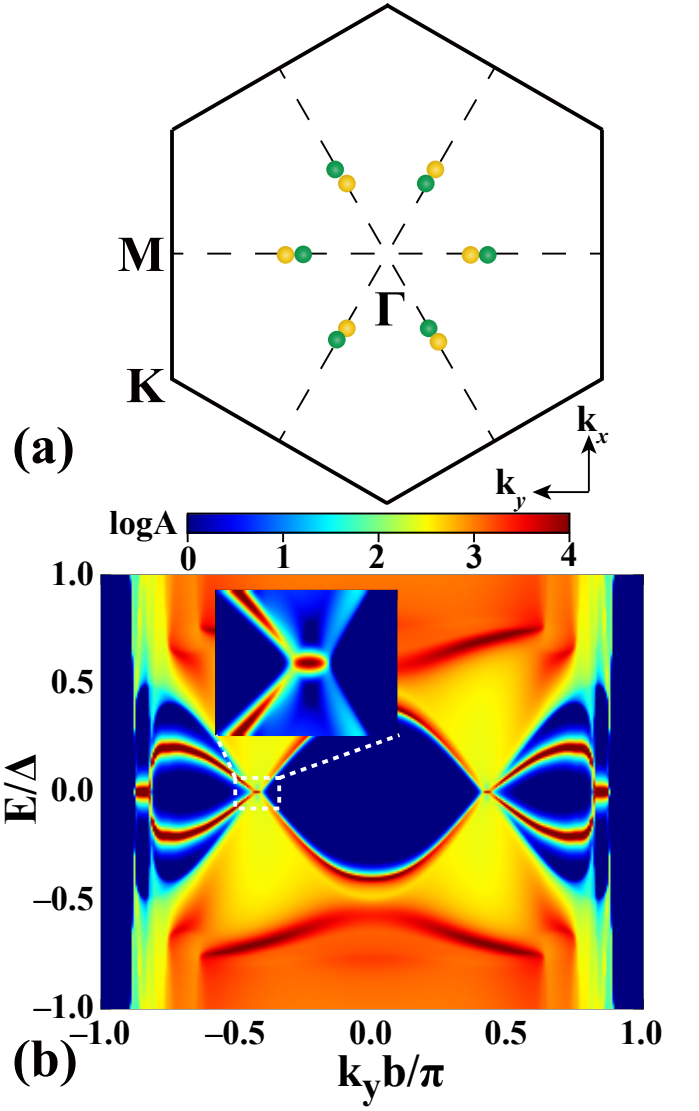


FIG. 2: The nodal topological superconducting monolayer NbSe₂ driven by in-plane magnetic field with $H = 3H_p$. (a) The position for the six pairs of point nodes. They project into four pairs of nodal points on the armchair edges as shown in (b). (b) The logarithmic plot of the spectral function $A(E, \mathbf{R})$ on the armchair edge of a semi-infinite strip of NbSe₂ with open boundary condition in the x -direction and periodic boundary condition in the y -direction. The Majorana flat bands connecting the point nodes at the sample edge. The insert shows a pair of nodal points connected by a Majorana flat band. Here $b = \sqrt{3}a$ and a the lattice constant

$\Gamma - M$ lines as dictated by symmetries, consistent with the calculations in Fig.1c.

Including the in-plane magnetic field, spin-singlet pairing, and in the basis of $[c_{k,\uparrow}, c_{k,\downarrow}, c_{-k,\uparrow}^\dagger, c_{-k,\downarrow}^\dagger]$, the Hamil-

tonian in the superconducting phase can be written as:

$$\mathcal{H}_s = \left[\frac{k_x^2 + k_y^2}{2m} - \mu \right] \tau_z + \lambda_{\text{SOC}} (k_+^3 + k_-^3) \sigma_z \quad (3)$$

$$+ \frac{1}{2} \mu_B g H_x \tau_z \sigma_x + \frac{1}{2} \mu_B g H_y \sigma_y + \Delta \tau_y \sigma_y.$$

Here, τ_i denotes Pauli matrices in the particle-hole basis. H_x and H_y are magnetic fields in the x- and y-directions respectively, μ_B is the Bohr magneton and g is the electron's gyromagnetic ratio. The pairing potential is denoted by Δ . Even though time-reversal is broken by the external magnetic field, \mathcal{H}_s respects a time-reversal like symmetry $U_T \mathcal{H}_s(k_x, k_y) U_T^{-1} = \mathcal{H}_s(-k_x, k_y)$ with $U_T = M_z T \tau_z$ and k_y unchanged under the symmetry operation. Moreover, \mathcal{H}_s respects a 1D particle-hole like symmetry $U_P \mathcal{H}_s(k_x, k_y) U_P^{-1} = -\mathcal{H}_s(-k_x, k_y)$ with $U_P = \tau_x K$. Therefore, for fixed k_y , \mathcal{H}_s respects the chiral symmetry $C \mathcal{H}_{k_y}(k_x) C^{-1} = -\mathcal{H}_{k_y}(k_x)$ where $C = \sigma_x \tau_y$. As a result, for any fixed k_y , \mathcal{H}_s is in the BDI class and the Hamiltonian can be topologically non-trivial [38–41]. For the range of k_y where \mathcal{H}_s is non-trivial, there are Majorana zero energy modes on the edge of the system as shown in Fig.2b. By tuning k_y as a parameter, the system can undergo a topological phase transition from a trivial regime to a non-trivial regime by closing the bulk gap. These topological phase transition k_y points are the nodal points in Fig.2b. The nodal points and the Majorana flat bands shown in Fig.2 can be reproduced by the simple Hamiltonian H_s in Eq.3.

Detection—In this section, we discuss the experimental detection of the nodal topological superconducting phase in NbSe₂. As discussed above, superconducting NbSe₂ can be driven from a fully gapped superconducting phase to a nodal superconducting phase by an in-plane magnetic field. As in the case of $d_{x^2-y^2}$ -wave superconductors, we expect the density of states of the system as a function of energy to be V-shape near zero energy when the system is nodal. From the low-energy bulk spectrum of the effective Hamiltonian \mathcal{H}_s , the density of states near zero energy can be found to be $N \frac{2\pi|E|}{v_x v_y}$, where E is the energy and v_x, v_y denote the Fermi velocity in the x, y-directions near the nodal points and N is the number of nodal points. Thus, the bulk density of states near zero energy is indeed linearly proportional to $|E|$.

Using the real space version of the six-band tight-binding model H_{BDG} defined in the Method Section and the Supplementary Material [32], including pairing and the in-plane magnetic field, we calculate the local density of states in the bulk of the sample.

$$\rho(E) = -\frac{1}{\pi} \text{Tr} [\text{Im} G^{\text{R}}(E)], \quad (4)$$

here $G^{\text{R}}(E) = (E + i\eta - H_{\text{BDG}})^{-1}$ is the retarded Green's function. The local density of states for a point in the bulk is shown in Fig.3a. When the applied in-plane

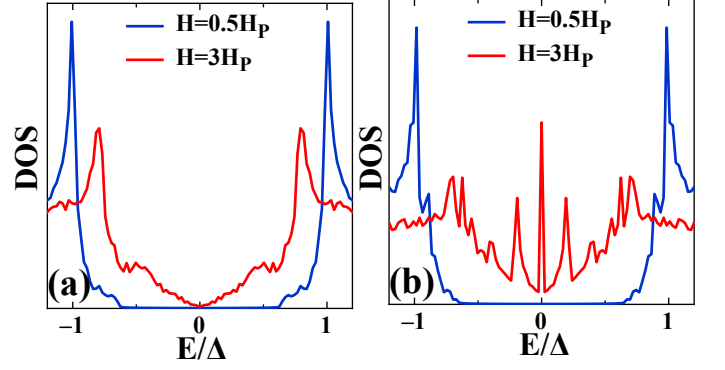


FIG. 3: (a) The local density of states (DOS) in the bulk in the fully gapped regime (blue curve) and the nodal regime (red curve) respectively. The in-plane magnetic field changes the DOS from U-shape ($H = 0.5H_P$) to V-shape ($H = 3H_P$). (b) The DOS on the armchair edge in the nodal topological phase with $H = 3H_P$. The zero energy DOS is strongly enhanced due to the zero energy Majorana modes associated with the Majorana flat bands (red curve).

field is lower than the Pauli limit, the density of states as a function of energy is U-shape (blue curve) near zero energy indicating a fully gapped superconducting state. On the other hand, the density of states is changed to V-shape (red curve) when the system is driven to the nodal phase as expected. Even though the V-shape density of states in the bulk is only the signature of a nodal phase, not necessarily a nodal topological phase, the observation of the fully gapped to nodal phase transition can be important for identifying the topological phase transition point.

Moreover, in the nodal topological phase, there are a large number of zero energy Majorana modes residing on the edges of the sample. These zero energy modes strongly enhance the local density of states on the edge of the superconductor. The local density of states at the edge of the sample, before and after the topological phase transition, are shown in Fig.3b. It is evident that, in the nodal topological phase with in-plane field stronger than the Pauli limit field, the zero energy density of states are strongly enhanced (red curve). Both the bulk density of states and the edge density of states can be detected by tunnelling spectroscopy experiments.

Interestingly, due to the zero energy Majorana modes, the pairing correlations induced on the edge of the superconductor are indeed spin-triplet. To show this, we calculated the pairing correlation for a site on the armchair edge of the sample. The pairing correlation can be parametrized as [9, 42, 43]:

$$F_{\sigma\sigma'}(E) = -i \sum_o \int_0^\infty e^{i(E+i0^+)t} \langle \{c_{\sigma,o}(t), c_{\sigma',o}(0)\} \rangle dt \quad (5)$$

where σ and o are the spin and orbital indices respectively. In the matrix form, the pairing correlation is writ-

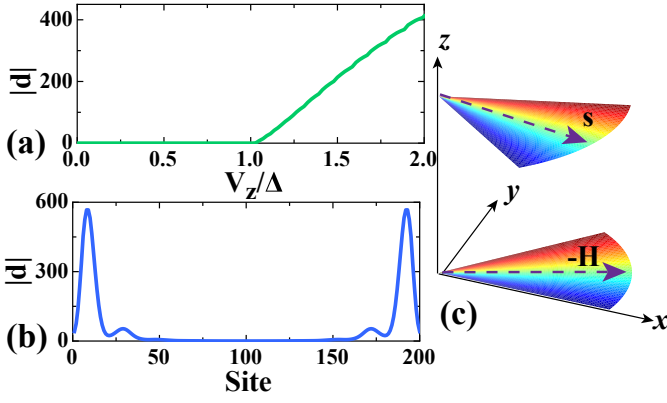


FIG. 4: (a) The triplet-pairing correlation amplitude $|d|$ on the armchair edge of the sample, as a function of V_z/Δ where $V_z = \frac{1}{2}\mu_B gH$. It becomes nonzero after the Majorana flat bands emerge when $V_z > \Delta$. (b) The spatial dependence of $|d|$ in the nodal topological phase with $H = 3H_P$. Here the sites are along the x -direction. (c) The spin polarization direction \mathbf{s} of the Cooper pair at the armchair edge. \mathbf{s} depends on the direction of the applied magnetic field \mathbf{H} . The vector \mathbf{s} with certain color is determined by the vector $-\mathbf{H}$ of the same color.

ten as:

$$F(E) = (\psi + \mathbf{d} \cdot \boldsymbol{\sigma}) i\sigma_y. \quad (6)$$

Here, the so-called \mathbf{d} -vector characterizes the triplet-pairing correlation and ψ characterizes the spin-singlet pairing correlation. In Fig.4a, it is shown that the triplet pairing correlation at zero energy on the armchair edge of the sample is non-zero only when the Zeeman energy $V_z = \frac{1}{2}\mu_B g|H|$ is larger than Δ . Fig.4b shows the spatial variation of $|d|$ across the sample for strip of NbSe₂ which has a width of 200-sites in the x -direction (perpendicular to the armchair edge). It is evident that $|d|$ is significant only near the two edges of the sample. On the other hand, the singlet pairing correlation amplitude ψ at zero energy is negligible. Furthermore, we calculated $\mathbf{s} = i(\mathbf{d} \times \mathbf{d}^*)/|\mathbf{d}|^2$ which gives the spin-polarization direction of the Cooper pairs [44] as shown in Fig.4c. This indicates that the Cooper pairs injected into the superconductor by the normal lead are spin-polarized with spin pointing to \mathbf{s} -direction [41, 45]. As a result, even though the lead attached to the superconductor is non-magnetic, the current from the lead to the superconductor is spin-polarized. We believe this property of monolayer NbSe₂ may lead to applications in superconducting spintronics [46, 47].

Discussion

We would like to discuss some important points about the nodal topological phase mentioned above. First, the large number of Majorana zero energy modes associated with the Majorana flat band in Fig.2b are protected against disorder. This is in sharp contrast to the $d_{x^2-y^2}$ -wave superconductor in which the zero energy fermionic

modes can be lifted to finite energy by disorder. One can show that the zero energy Majorana modes is not protected by the bulk gap (since the system is nodal) but by the chiral symmetry $C = \sigma_x \tau_y$ of H_s in Eq.3 [48]. This chiral symmetry is not broken by on-site disorders. This is similar to the toy model studied in Ref. [40], where an in-plane magnetic field creates Majorana flat bands in a time-reversal invariant $p \pm ip$ topological superconductor.

Second, we emphasize that the Γ pocket is essential for creating the nodal topological phase. In the case of gated MoS₂ or WS₂, superconductivity appear in the conduction bands near the K pockets only. Therefore, the nodal phase discussed above cannot be found in those superconductors. On the other hand, intrinsic superconductors NbSe₂, NbS₂, TaSe₂ and TaS₂ are candidate materials for realizing the nodal topological superconducting phase found in this work.

Third, the armchair edge is not essential for the observation of the Majorana flat bands as long as the edge is not parallel to the zig-zag edge (k_x direction in Fig.2a). On the zig-zag edge, the projection of the bulk nodal points can cancel each other such that there are no topologically non-trivial regimes for all k_x parallel to the zig-zag edge. For all other edges, one can find finite sections of Majorana flat bands along the edges when the system is driven to the nodal topological phase.

Method

Tight-binding Hamiltonians—In the basis of $[c_{\mathbf{k}, d_{z^2}, \uparrow}, c_{\mathbf{k}, d_{xy}, \uparrow}, c_{\mathbf{k}, d_{x^2-y^2}, \uparrow}, c_{\mathbf{k}, d_{z^2}, \downarrow}, c_{\mathbf{k}, d_{xy}, \downarrow}, c_{\mathbf{k}, d_{x^2-y^2}, \downarrow}]$, the six-band model used has the form [2]

$$H_N(\mathbf{k}) = H_{\text{TNN}}(\mathbf{k}) \otimes \sigma_0 + \frac{1}{2}\lambda L_z \otimes \sigma_z + I_3 \otimes \frac{1}{2}\mu_B g \mathbf{H} \cdot \boldsymbol{\sigma} \quad (7)$$

with

$$H_{\text{TNN}}(\mathbf{k}) = \begin{pmatrix} V_0 & V_1 & V_2 \\ V_1^* & V_{11} & V_{12} \\ V_2^* & V_{12}^* & V_{22} \end{pmatrix}, L_z = \begin{pmatrix} 0 & 0 & 0 \\ 0 & 0 & -i \\ 0 & i & 0 \end{pmatrix} \quad (8)$$

where I_n means the $n \times n$ identity matrix. The details about these matrix elements can be found in supplementary material [32]. Then the Bogliubov-de Gennes Hamiltonian in Nambu spinor representation can be written as

$$H_{\text{BdG}}(\mathbf{k}) = \begin{pmatrix} H_N(\mathbf{k}) - \mu I_6 & -i\Delta \sigma_y \otimes I_3 \\ i\Delta \sigma_y \otimes I_3 & -H_N^*(-\mathbf{k}) + \mu I_6 \end{pmatrix}. \quad (9)$$

The real space version of H_{TNN} and H_{BdG} can be found in the Supplementary Material [32].

Acknowledgement—The authors thank Patrick A. Lee, Masatoshi Sato and Noah F. Q. Yuan for insightful discussions. W. -Y. H acknowledges the support of Hong Kong PhD Fellowship. K. T. L thanks the support of HKRGC and Croucher Foundations through

HKUST3/CRF/13G, 602813, 605512, 16303014 and Croucher Innovation Grants.

* phlaw@ust.hk

- [1] Mattheiss, L. F. Band Structures of Transition-Metal-Dichalcogenide Layer Compounds, *Phys. Rev. B* **8**, 3719 (1973).
- [2] Radisavljevic, B., Radenovic, A., Brivio, J., Giacometti, V. & Kis, A. Single-layer MoS₂ transistors, *Nat. Nanotechnol.* **6**, 147-150 (2011).
- [3] Zhang, Y.-J., Ye, J.-T., Matsushashi, Y. & Iwasa, Y. Ambipolar MoS₂ Thin Flake Transistors, *Nano Lett.* **12**, 1136-1140 (2012).
- [4] Wang, Q. H., Kalantar-Zadeh, K., Kis, A., Coleman, J. N. & Strano, M. S. Electronics and optoelectronics of two-dimensional transition metal dichalcogenides, *Nat. Nanotechnol.* **7**, 699-712 (2012).
- [5] Bao, W., Cai, X., Kim, D., Sridhara, D. & Fuhrer, M. S. High mobility ambipolar MoS₂ field-effect transistors: Substrate and dielectric effects, *Appl. Phys. Lett.* **102**, 042104 (2013).
- [6] Mak, K. F., He, K., Lee, C., Lee, G. H., Hone, J., Heinz, T. F. & Shan, J. Tightly bound trions in monolayer MoS₂, *Nat. Mater.* **12**, 207-211 (2013).
- [7] Lu, J. M., Zheliuk, O., Leermakers, I., Yuan, N. F. Q., Zeitler, U., Law, K. T. & Ye, J. T. Evidence for two-dimensional Ising superconductivity in gated MoS₂, *Science* **350**, 1353-1357 (2015).
- [8] Xi, X., Wang, Z., Zhao, W., Park, J.-H., Law, K. T., Berger, H., Forro, L., Shan, J. & Mak, K. F. Ising pairing in superconducting NbSe₂ atomic layers, *Nat. Phys.* **12**, 139-143 (2016).
- [9] Zhou, T., Jiang, H.-L., Yuan, Noah. F. Q. & Law, K. T. Ising Superconductivity and Majorana Fermions in Transition Metal Dichalcogenides, <http://arxiv.org/abs/1510.06289> (2015).
- [10] Rashba, E. I. Symmetry of bands in wurzite-type crystals. 1. Symmetry of bands disregarding spin-orbit interaction, *Sov. Phys. Solid. State* **1**, 368 (1959).
- [11] Zeng, H. L., Liu, G.-B., Dai, J. F., Yan, Y. J., Zhu, B. R., He, R. C., Xie, L., Xu, S. J., Chen, X. H., Yao, W. & Cui, X. D. Optical signature of symmetry variations and spin-valley coupling in atomically thin tungsten dichalcogenides, *Sci. Rep.* **3**, 1608 (2013).
- [12] Yuan, H. T. et al. Zeeman-type spin splitting controlled by an electric field, *Nat. Phys.* **9**, 563-569 (2013).
- [13] Liu, G.-B., Shan, W.-Y., Yao, Y., Yao, W. & Xiao, D. Three-band tight-binding model for monolayers of group-VIB transition metal dichalcogenides, *Phys. Rev. B* **88**, 085433 (2013).
- [14] Xiao, D., Liu, G.-B., Feng, W., Xu, X. & Yao, W. Coupled Spin and Valley Physics in Monolayer MoS₂ and Other Group-VI Dichalcogenides, *Phys. Rev. Lett.* **108**, 196802 (2012).
- [15] Mak, K. F., He, K., Shan, J. & Heinz, T. F. Control of valley polarization in monolayer MoS₂ by optical helicity, *Nat. Nanotechnol.* **7**, 494-498 (2012).
- [16] Zeng, H., Dai, J., Yao, W., Xiao, D. & Cui, X. Valley polarization in MoS₂ monolayers by optical pumping, *Nat. Nanotechnol.* **7**, 490-493 (2012).
- [17] Ye, J. T., Zhang, Y. J., Akashi, R., Bahramy, M. S., Arita, R. & Iwasa, Y. Superconducting Dome in Gate-Tuned Band Insulator, *Science* **338**, 1193-1196 (2012).
- [18] Taniguchi, K., Matsumoto, A., Shimotani, H. & Takagi, H. Electric-field-induced superconductivity at 9.4K in a layered transition metal disulphide MoS₂, *Appl. Phys. Lett.* **101**, 042603 (2012).
- [19] Shi, W., Ye, J. T., Zhang, Y., Suzuki, R., Yoshida, M., Miyazaki, J., Inoue, N., Saito, Y. & Iwasa, Y. Superconductivity Series in Transition Metal Dichalcogenides by Ionic Gating, *Scientific Reports* **5**, 12534 (2015).
- [20] Saito, Y., Nakamura, Y., Bahramy, M. S., Kohama, Y., Ye, J., Kasahara, Y., Nakagawa, Y., Onga, M., Tokunaga, M., Nojima, T., Yanase, Y. & Iwasa, Y. Superconductivity protected by spin-valley locking in ion-gated MoS₂, *Nat. Phys.* **12**, 144-149 (2016).
- [21] Sharma, G. & Tewari, S. Yu-Shiba-Rusinov states and topological superconductivity in Ising paired superconductors, <https://arxiv.org/abs/1603.08909> (2016).
- [22] Zhang, J. & Aji, V. Topological Yu-Shiba-Rusinov chain in monolayer transition-metal dichalcogenide superconductors, <http://arxiv.org/abs/1604.02134> (2016).
- [23] Xi, X., Zhao, L., Wang, Z., Berger, H., Forro, L., Shan, J. & Mak, K. F. Strongly enhanced charge-density-wave order in monolayer NbSe₂, *Nat. Nanotechnol.* **10**, 765-769 (2015).
- [24] Ugeda, M. M. et al. Characterization of collective ground states in single-layer NbSe₂, *Nat. Phys.* **12** 92-97 (2016).
- [25] Tsen, A. W., Hunt, B., Kim, Y. D., Yuan, Z. J., Jia, S., Cava, R. J., Hone, J., Kim, P., Dean, C. R. & Pasupathy, A. N. Nature of the quantum metal in two-dimensional crystalline superconductor, *Nat. Phys.* **12**, 208-212 (2016).
- [26] Xu, S.-Y. et al. Discovery of a Weyl fermion semimetal and topological Fermi arcs, *Science* **349**, 613-617 (2015).
- [27] Weng, H., Fang, C., Fang, Z., Bernevig, B. A. & Dai, X. Weyl Semimetal Phase in Noncentrosymmetric Transition-Metal Monophosphides, *Phys. Rev. X* **5**, 011029 (2015).
- [28] Yang, L. X., Liu, Z. K., Sun, Y., Peng, H., Yang, H. F., Zhang, T., Zhou, B., Zhang, Y., Guo, Y. F., Rahn, M., Prbnakaran, D., Hussain, Z., Mo, S.-K., Felser, C., Yan, B. & Chen, Y. L. Weyl semimetal phase in the non-centrosymmetric compounds TaAs, *Nat. Phys.* **11**, 728-732 (2015).
- [29] Yuan, N. F. Q., Mak, K. F. & Law, K. T. Possible Topological Superconducting Phases of MoS₂, *Phys. Rev. Lett.* **113**, 097001 (2014).
- [30] Here the ABINIT code is used to perform the calculation for the band structure of monolayer NbSe₂. See also the web page at <http://www.abinit.org>.
- [31] Lebegue, S. & Eriksson, O. Electronic structure of two-dimensional crystal from *ab initio* theory, *Phys. Rev. B* **79**, 115409 (2009).
- [32] The supplementary information for the details of the tight binding model.
- [33] Revolinsky, E., Spiering, G. A. & Beernsten, D. J. Superconductivity in the niobium-selenium system, *J. Phys. Chem. Solids* **26**, 1029-1034 (1965).
- [34] Toyota, N. et al. Temperature and angular dependences of upper critical fields for the layer structure superconductor 2H-NbSe₂, *J. Low. Temp. Phys.* **25**, 485-499 (1976).
- [35] Clogston, A. M. Upper Limit for the Critical Field in Hard Superconductors, *Phys. Rev. Lett.* **9**, 266 (1962).
- [36] K. F. Mak, private communications.

- [37] Huertas-Hernando, D., Guinea, F. & Brataas, A. Spin-orbit coupling in curved graphene, fullerenes, nanotubes, and nanotube caps, *Phys. Rev. B* **74**, 155426 (2006).
- [38] Schnyder, A. P., Ryu, S., Furusaki, A. & Ludwig, A. W. W. Classification of topological insulators and superconductors in three spatial dimensions, *Phys. Rev. B* **78**, 195125 (2008).
- [39] Tewari S. & Sau, J. D. Topological Invariants for Spin-Orbit Coupled Superconductor Nanowires, *Phys. Rev. Lett.* **109**, 150408 (2012).
- [40] Wong, C. L. M., Liu, J., Law, K. T. & Lee, P. A. Majorana flat bands and unidirectional Majorana edge states in gapless topological superconductors, *Phys. Rev. B* **88**, 060504 (R) (2013).
- [41] Yuan, N. F. Q., Lu, Y., He, J. J. & Law, K. T. Generating Giant Spin Currents Using Nodal Topological Superconductors, <http://arxiv.org/abs/1510.03137> (2015).
- [42] Gor'kov, L. P. & Rashba, E. I. Superconducting 2D System with Lifted Spin Degeneracy: Mixed Singlet-Triplet State, *Phys. Rev. Lett.* **87**, 037004 (2011).
- [43] Frigeri, P. A., Agterberg, D. F. & Sigrist, M. Spin susceptibility in superconductors without inversion symmetry, *New J. of Phys.* **6** 115 (2004).
- [44] Leggett, A. J. A theoretical description of the new phases of liquid ^3He , *Rev. Mod. Phys.* **47**, 331-414 (1976).
- [45] He, J. J., Ng, T. K., Lee, P. A. & Law, K. T. Selective Equal-Spin Andreev Reflections Induced by Majorana Fermions, *Phys. Rev. Lett.* **112**, 037001 (2014).
- [46] Linder, J. & Robinson, J. W. A. Superconducting spintronics, *Nat. Phys.* **11**, 307-315 (2015).
- [47] Eschrig, M. Spin-polarized supercurrents for spintronics, *Phys. Today* **64**, 43-49 (January 2011).
- [48] Sato, M., Tanaka, Y., Yada, K. & Yokoyama, T. Topology of Andreev bound states with flat dispersion, *Phys. Rev. B* **83**, 224511 (2011).

Supplementary Material: Nodal Topological Superconductivity in Monolayer NbSe₂

I. TIGHT BINDING MODEL

The valence band of monolayer NbSe₂ is dominated by the d_{z^2} , d_{xy} and $d_{x^2-y^2}$ orbitals from Nb atoms [S1, S2]. In the basis of $[c_{\mathbf{k},d_{z^2},\uparrow}, c_{\mathbf{k},d_{xy},\uparrow}, c_{\mathbf{k},d_{x^2-y^2},\uparrow}, c_{\mathbf{k},d_{z^2},\downarrow}, c_{\mathbf{k},d_{xy},\downarrow}, c_{\mathbf{k},d_{x^2-y^2},\downarrow}]$, the corresponding normal state tight binding model up to the third-nearest-neighbor hopping can be written as

$$H_N(\mathbf{k}) = H_{\text{TNN}}(\mathbf{k}) \otimes \sigma_0 + \frac{1}{2} \lambda L_z \otimes \sigma_z + I_3 \otimes \mathbf{H} \cdot \boldsymbol{\sigma} \quad (\text{S1})$$

with

$$H_{\text{TNN}}(\mathbf{k}) = \begin{pmatrix} V_0 & V_1 & V_2 \\ V_1^* & V_{11} & V_{12} \\ V_2^* & V_{12}^* & V_{22} \end{pmatrix}, L_z = \begin{pmatrix} 0 & 0 & 0 \\ 0 & 0 & -i \\ 0 & i & 0 \end{pmatrix} \quad (\text{S2})$$

where I_3 is the 3×3 identity matrix. Defining $(\alpha, \beta) = \left(\frac{1}{2}k_x a, \frac{\sqrt{3}}{2}k_y a\right)$, V_0 , V_1 , V_2 , V_{11} , V_{12} and V_{22} can be expressed as

$$V_0 = \epsilon_1 + 2t_0 (2 \cos \alpha \cos \beta + \cos 2\alpha) + 2r_0 (2 \cos 3\alpha \cos \beta + \cos 2\beta) + 2u_0 (2 \cos 2\alpha \cos 2\beta + \cos 4\alpha), \quad (\text{S3})$$

$$\text{Re}[V_1] = -2\sqrt{3}t_2 \sin \alpha \sin \beta + 2(r_1 + r_2) \sin 3\alpha \sin \beta - 2\sqrt{3}u_2 \sin 2\alpha \sin 2\beta, \quad (\text{S4})$$

$$\text{Im}[V_1] = 2t_1 \sin \alpha (2 \cos \alpha + \cos \beta) + 2(r_1 - r_2) \sin 3\alpha \cos \beta + 2u_1 \sin 2\alpha (2 \cos 2\alpha + \cos 2\beta), \quad (\text{S5})$$

$$\text{Re}[V_2] = 2t_2 (\cos 2\alpha - \cos \alpha \cos \beta) - \frac{2}{\sqrt{3}} (r_1 + r_2) (\cos 3\alpha \cos \beta - \cos 2\beta) + 2u_2 (\cos 4\alpha - \cos 2\alpha \cos 2\beta), \quad (\text{S6})$$

$$\text{Im}[V_2] = 2\sqrt{3}t_1 \cos \alpha \sin \beta + \frac{2}{\sqrt{3}} (r_1 - r_2) \sin \beta (\cos 3\alpha + 2 \cos \beta) + 2\sqrt{3}u_1 \cos 2\alpha \sin 2\beta, \quad (\text{S7})$$

$$V_{11} = \epsilon_2 + (t_{11} + 3t_{22}) \cos \alpha \cos \beta + 2t_{11} \cos 2\alpha + 4r_{11} \cos 3\alpha \cos \beta + 2(r_{11} + \sqrt{3}r_{12}) \cos 2\beta \quad (\text{S8})$$

$$+ (u_{11} + 3u_{22}) \cos 2\alpha \cos 2\beta + 2u_{11} \cos 4\alpha, \quad (\text{S9})$$

$$\text{Re}[V_{12}] = \sqrt{3}(t_{22} - t_{11}) \sin \alpha \sin \beta + 4r_{12} \sin 3\alpha \sin \beta + \sqrt{3}(u_{22} - u_{11}) \sin 2\alpha \sin 2\beta, \quad (\text{S10})$$

$$\text{Im}[V_{12}] = 4t_{12} \sin \alpha (\cos \alpha - \cos \beta) + 4u_{12} \sin 2\alpha (\cos 2\alpha - \cos 2\beta), \quad (\text{S11})$$

and

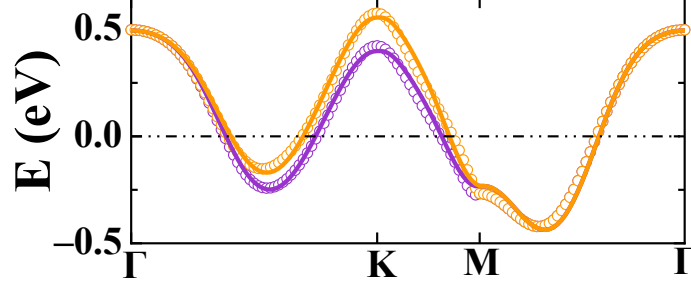
$$V_{22} = \epsilon_2 + (3t_{11} + t_{22}) \cos \alpha \cos \beta + 2t_{22} \cos 2\alpha + 2r_{11} (2 \cos 3\alpha \cos \beta + \cos 2\beta) \\ + \frac{2}{\sqrt{3}} r_{12} (4 \cos 3\alpha \cos \beta - \cos 2\beta) + (3u_{11} + u_{22}) \cos 2\alpha \cos 2\beta + 2u_{22} \cos 4\alpha. \quad (\text{S12})$$

The specific parameters in this third-nearest-neighbor tight binding model can be fitted from the band structure by first principle and are summarized in Table I. It can be seen from Fig. S1 that the third-nearest-neighbor tight binding model matches well with the first principle calculation results. Then the Bogliubov-de Gennes Hamiltonian in Nambu spinor representation can be written as

$$H_{\text{BdG}}(\mathbf{k}) = \begin{pmatrix} H_N(\mathbf{k}) - \mu \sigma_0 \otimes I_3 & -i\Delta \sigma_y \otimes I_3 \\ i\Delta \sigma_y \otimes I_3 & -H_N^*(-\mathbf{k}) + \mu \sigma_0 \otimes I_3 \end{pmatrix}. \quad (\text{S13})$$

TABLE I: Fitting parameters for the Hamiltonian $H_{\text{TNN}}(\mathbf{k})$. The energy parameters ϵ_1 to λ are in units of eV.

ϵ_1	ϵ_2	t_0	t_1	t_2	t_{11}	t_{12}	t_{22}	r_0	r_1
r_2	r_{11}	r_{12}	u_0	u_1	u_2	u_{11}	u_{12}	u_{22}	λ
1.4466	1.8496	-0.2308	0.3116	0.3459	0.2795	0.2787	-0.0539	0.0037	-0.0997
0.0385	0.0320	0.0986	0.0685	-0.0381	0.0535	0.0601	-0.0179	-0.0425	0.0784

FIG. S1: The band structure for the normal state of monolayer NbSe₂. The circles represent the first principle calculation results, while the solid lines are the tight binding results.

II. MODEL FOR ARMCHAIR NANORIBBON

In this section, we apply the third-nearest-neighbor tight binding model to study the superconducting monolayer NbSe₂ nano-ribbon. Taking the armchair direction along y , we have N Nb atoms in one unit cell as shown in Fig. S2. With periodic boundary conditions in the y direction and open boundary conditions in the x direction, the $6N \times 6N$ Hamiltonian matrix for the normal state armchair nano-ribbon can be obtained as follows

$$H_{\text{ribbon}}(k_y) = I_2 \otimes H_0 + \sigma_z \otimes I_N \otimes \frac{1}{2}\lambda L_z + \mathbf{H} \cdot \boldsymbol{\sigma} \otimes I_{3N}. \quad (\text{S14})$$

where I_n ($n = 2, N, 3N$) means the $n \times n$ identity matrix and H_0 reads

$$H_0 = \begin{pmatrix} h_1 & h_2 & h_3 & h_4 & h_5 & 0 & \cdots & 0 \\ h_2^\dagger & h_1 & h_2 & h_3 & h_4 & h_5 & & \vdots \\ h_3^\dagger & h_2^\dagger & h_1 & h_2 & \ddots & \ddots & \ddots & 0 \\ h_4^\dagger & h_3^\dagger & h_2^\dagger & \ddots & \ddots & \ddots & \ddots & h_4 & h_5 \\ h_5^\dagger & h_4^\dagger & \ddots & \ddots & \ddots & \ddots & \ddots & h_3 & h_4 \\ 0 & h_5^\dagger & \ddots & \ddots & \ddots & h_1 & h_2 & h_3 \\ \vdots & & \ddots & h_4^\dagger & h_3^\dagger & h_2^\dagger & h_1 & h_2 \\ 0 & \cdots & 0 & h_5^\dagger & h_4^\dagger & h_3^\dagger & h_2^\dagger & h_1 \end{pmatrix}_{N \times N}. \quad (\text{S15})$$

Here h_n ($n = 1, 2, 3, 4, 5$), the hopping matrix between different sites reads

$$h_1 = \begin{pmatrix} \epsilon_1 + 2r_0 \cos 2\beta & 0 & \frac{2(r_1+r_2)}{\sqrt{3}} \cos 2\beta + i \frac{2(r_1-r_2)}{\sqrt{3}} \sin 2\beta \\ 0 & \epsilon_2 + 2(r_{11} + \sqrt{3}r_{12}) \cos 2\beta & 0 \\ \frac{2(r_1+r_2)}{\sqrt{3}} \cos 2\beta - i \frac{2(r_1-r_2)}{\sqrt{3}} \sin 2\beta & 0 & \epsilon_2 + (2r_{11} - \frac{2}{\sqrt{3}}r_{12}) \cos 2\beta \end{pmatrix}, \quad (\text{S16})$$

$$h_2 = \begin{pmatrix} 2t_0 \cos \beta & -i\sqrt{3}t_2 \sin \beta - t_1 \cos \beta & -t_2 \cos \beta + i\sqrt{3}t_1 \sin \beta \\ -i\sqrt{3}t_2 \sin \beta + t_1 \cos \beta & \frac{1}{2}(t_{11} + 3t_{22}) \cos \beta & i\frac{\sqrt{3}}{2}(t_{22} - t_{11}) \sin \beta + 2t_{12} \cos \beta \\ -t_2 \cos \beta - i\sqrt{3}t_1 \sin \beta & i\frac{\sqrt{3}}{2}(t_{22} - t_{11}) \sin \beta - 2t_{12} \cos \beta & \frac{1}{2}(3t_{11} + t_{22}) \cos \beta \end{pmatrix}, \quad (\text{S17})$$

$$h_3 = \begin{pmatrix} t_0 + 2u_0 \cos 2\beta & -t_1 - i\sqrt{3}u_2 \sin 2\beta - u_1 \cos 2\beta & t_2 - u_2 \cos 2\beta + i\sqrt{3}u_1 \sin 2\beta \\ t_1 - i\sqrt{3}u_2 \sin 2\beta + u_1 \cos 2\beta & t_{11} + \frac{1}{2}(u_{11} + 3u_{22}) \cos 2\beta & -t_{12} + 2u_{12} \cos 2\beta + i\frac{\sqrt{3}}{2}(u_{22} - u_{11}) \sin 2\beta \\ t_2 - u_2 \cos 2\beta - i\sqrt{3}u_1 \sin 2\beta & t_{12} - 2u_{12} \cos 2\beta + i\frac{\sqrt{3}}{2}(u_{22} - u_{11}) \sin 2\beta & t_{22} + \frac{1}{2}(3u_{11} + u_{22}) \cos 2\beta \end{pmatrix}, \quad (\text{S18})$$

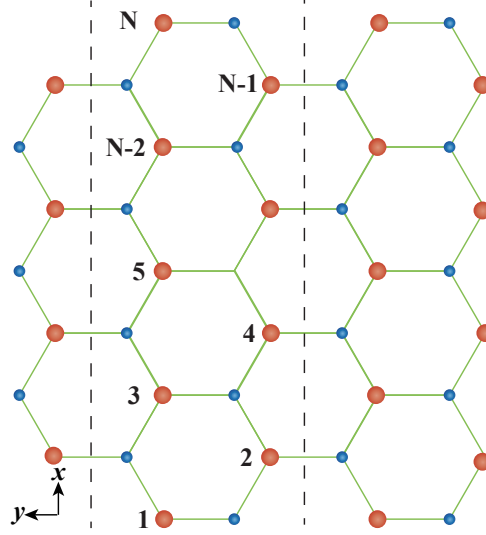


FIG. S2: The unit cell NbSe₂ nano-ribbon with armchair edge.

$$h_4 = \begin{pmatrix} 2r_0 \cos \beta & i(r_1+r_2) \sin \beta - (r_1-r_2) \cos \beta - \frac{r_1+r_2}{\sqrt{3}} \cos \beta + i \frac{r_1-r_2}{\sqrt{3}} \sin \beta \\ i(r_1+r_2) \sin \beta + (r_1-r_2) \cos \beta & 2r_{11} \cos \beta & i2r_{12} \sin \beta \\ -\frac{r_1+r_2}{\sqrt{3}} \cos \beta - i \frac{r_1-r_2}{\sqrt{3}} \sin \beta & i2r_{12} \sin \beta & (2r_{11} + 4 \frac{r_{12}}{\sqrt{3}}) \cos \beta \end{pmatrix}, \quad (\text{S19})$$

$$h_5 = \begin{pmatrix} u_0 & -u_1 & u_2 \\ u_1 & u_{11} & -u_{12} \\ u_2 & u_{12} & u_{22} \end{pmatrix}. \quad (\text{S20})$$

In this way the Bogliubov-de Gennes Hamiltonian for the superconducting monolayer NbSe₂ ribbon can be obtained as

$$H_{\text{ribbon}}^{\text{BdG}} = \begin{pmatrix} H_{\text{ribbon}}(k_y) - \mu I_{6N} & -i\sigma_y \Delta \otimes I_{3N} \\ i\sigma_y \Delta \otimes I_{3N} & -H_{\text{ribbon}}^*(-k_y) + \mu I_{6N} \end{pmatrix}. \quad (\text{S21})$$

With this Hamiltonian, the spectral function $A = \text{Tr}[\text{Im}G(E, \mathbf{R})]$ for the semi-infinite NbSe₂ ribbon with armchair edge is calculated in Fig. 2. Here \mathbf{R} is the last slab of the NbSe₂ ribbon and the Green's function $G = (E + i0^+ - H_{\text{ribbon}}^{\text{BdG}})^{-1}$ can be obtained through the surface Green function method [S3]. We set $\Delta = 0.02\text{eV}$ in Fig. 2-4 of the main text.

* phlaw@ust.hk

[S1] S. Lebegue and O. Eriksson, Phys. Rev. B **79**, 115409 (2009).

[S2] G.-B. Liu, W.-Y. Shan, Y. Yao, W. Yao and D. Xiao, Phys. Rev. B **88**, 085433 (2013).

[S3] S. Datta, Quantum Transport (Cambridge University Press, Cambridge, New York, 2005).